Coupling threshold theory and satellite image derived channel width to estimate the formative discharge of Himalayan Foreland rivers.

Kumar Gaurav[1], François Métivier[2], AV Sreejith[3], Rajiv Sinha[4], Amit Kumar[1], and Sampat Kumar Tandon[1]

[1]Indian Institute of Science Education and Research, Bhopal,462066, M.P, India
[2]Institute de Physique du Globe de Paris, 1 Rue Jussieu, 75005 Paris cedex 05, France
[3]School of Mathematics and Computer Science, Indian Institute of Technology, Goa, 403401, Goa, India
[4]Department of Earth Sciences, Indian Institute of Technology, Kanpur, 208016 UP, India

Correspondence: K.Gaurav (kgaurav@iiserb.ac.in)

Abstract. We propose an innovative methodology to estimate the formative discharge of alluvial rivers from remote sensing images. This procedure involves automatic extraction of the width of a channel from Landsat Thematic Mapper, Landsat 8, and Sentinel-1 satellite images. We translate the channel width extracted from satellite images to discharge by using a width-discharge regime curve established previously by us for the Himalayan Rivers. This regime curve is based on the threshold

5 theory, a simple physical force balance that explains the first-order geometry of alluvial channels. Using this procedure, we estimate the discharge of six major rivers of the Himalayan Foreland: the Brahmaputra, Chenab, Ganga, Indus, Kosi, and Teesta rivers. Except highly regulated rivers (Indus and Chenab), our estimates of the discharge from satellite images can be compared with the mean annual discharge obtained from historical records of gauging stations. We have shown that this procedure applies both to braided and single-thread rivers over a large territory. Further our methodology to estimate discharge

10 from remote sensing images does not rely on continuous ground calibration.

Keywords: Himalayan Foreland; regime curve; threshold theory; formative discharge

1 Introduction

15 The measurement of river discharge is necessary to investigate channel morphology, sediment transport, flood risks, and to assess water resources. Despite this, the discharge of many rivers remains unknown, especially those located in sparsely populated regions, at high latitudes, or in developing countries. Even now, the discharge is measured at sparsely located stations along a river's course (Smith and Pavelsky, 2008; Andreadis et al., 2007). Between measurement stations, the discharge is interpolated using routine techniques (Smith and Pavelsky, 2008). Further, these local measurement stations are installed where

20 the river flows as a single-thread channel and has a stable boundary. This is often not the case for braided rivers, where the flow

is distributed through multiple and mobile threads (Smith et al., 1996; Ashmore and Sauks, 2006). Braided rivers are therefore often not gauged; and where these exist, the gauging stations are located at places like dams with artificially regulated flow. This hinders our ability to assess discharge in the individual threads of a braided river.

To overcome this problem, and to minimise the costs related to discharge measurement, methodologies have been developed
25 to use remote sensed images to estimate the instantaneous discharge of rivers (Smith et al., 1996; Smith, 1997; Alsdorf et al., 2000; Ashmore and Sauks, 2006; Alsdorf et al., 2007; Marcus and Fonstad, 2008; Papa et al., 2010, 2012; Gleason and Smith, 2014; Durand et al., 2016; Gleason et al., 2018; Allen and Pavelsky, 2018; Moramarco et al., 2019; Kebede et al., 2020). These studies establish rating relationships between some image-derived parameters (width, water level or stage, slope), to the instantaneous discharge measured in the field (Leopold and Maddock, 1953). Equations that define the hydraulic geometry of
30 a channel relate width (W), average depth (H), and slope (S) of a channel to its discharge (Q) according to:

$$W = aQ^e, \tag{1}$$
$$H = bQ^f, \tag{2}$$
$$S = cQ^{-g}, \tag{3}$$

where a, b, c, e, f, g are site specific constants and exponents. The available methods, based on remote sensing data, to es-
35 timate the discharge of a river therefore cannot be extrapolated to other rivers, or even to other locations on the same river. Moreover, as these rating curves vary significantly between locations, they must be established for each location independently. For example, Smith et al. (1995); Smith (1997); Smith and Pavelsky (2008) and Ashmore and Sauks (2006), used synthetic aperture radar and ortho-rectified aerial images to estimate discharge in braided rivers. They related the image derived effective width of a braided river to the discharge at a nearby gauge station to establish a relationship of the form of equations 1, 2, & 3.
40 Their approach provides an estimate of the total discharge in a braided river, at a given section. However, this technique is site specific and assumes that the river bed does not change over time.

Few attempts have been made to overcome these limitations; for example Bjerklie et al. (2005) used aerial orthophotographs and SAR images to estimate discharge in various single-thread and braided rivers. To estimate the discharge they extracted the maximum water width at a given river reach. They then combined the image-derived channel widths with channel slopes
45 obtained from topographic maps, and a statistical hydrologic model. They reported standard errors of $50 - 100\%$. However, after using a calibration function based on field observation, the error reduced to values as low as 10%. Later, Sun et al. (2010) used Japan Earth Resource Satellite-1 (JERS-1) SAR images to measure the effective width of the Mekong River at the Pakse gauging station in Laos. They used rainfall-runoff model to estimate the discharge from the image-derived width and suggested that using this procedure, the discharge could be estimated in any ungauged river basin within an acceptable level of accuracy.
50 They established a close agreement between the measured discharge of the Mekong River at Paske station and the model estimate to the 90% uncertainty level. As discussed earlier by Bjerklie et al. (2005), later Sun et al. (2010) indicated that the precision can be improved by calibrating the rainfall-runoff model with a hydraulic geometry relation, and that a calibrated rainfall-runoff model can be used to estimate the discharge in any ungauged river using the measured width only. Gleason and

Smith (2014) have suggested that the discharge of a single-thread river can be estimated from satellite images only, without

55   any ground measurement. They plotted the exponents and coefficients of hydraulic regime equations established at 88 different gauging stations along six rivers in the United States, and found that the exponents and coefficients are correlated. Recently Kebede et al. (2020) have used Landsat images to estimate daily discharge of the Lhasa River in the Tibetan Plateau. They have used image derived hydraulic variables to compute the discharge by using modified Manning equation and rating curves established from the in-situ measurement of width and discharge.

60   The studies discussed above attempt to address the issue of site-specificity, and propose methods to estimate discharge without empirical calibration. However Bjerklie et al. (2005), and Sun et al. (2010) also show that a better accuracy in discharge prediction can only be achieved with some calibration to ground measurements. Therefore, a physically robust method to resolve the site-specificity of rating curves remains to be described.

To address this issue of site-specificity, we have developed a semi-empirical width-discharge regime relation based on

65   the threshold theory and field measurement of various braided and meandering rivers on the Ganga and Brahmaputra plain (Seizilles et al., 2013; Métivier et al., 2016; Gaurav et al., 2017). According to this relation, threads of braided and meandering rivers share a common width-discharge regime relationship. We therefore hypothesise that, this "unique" regime equation can be used to estimate the first order discharge of any river (braided or meandering) flowing on the Ganga and Brahmaputra plains, and perhaps on the entire Himalayan Foreland, if width of the river channels is known. This study can also be used for various

70   applications such as: (i) to monitor the downstream evolution of discharge, (ii) to fill the data gap in between the gauge stations separated over a long distance, (iii) to construct the time-series and trend analysis of discharge variation, and (iv) to identify the critical reaches in rivers that are under stress due to excessive extraction of water for agriculture, industrial or domestic supply.

2   Hydrology of the Himalayan Rivers

Many rivers flowing on the Indus-Ganga-Brahmaputra alluvial plains are perennial and have their source in the Himalaya

75   and Tibetan Plateau. Flow of these rivers is primarily determined by snowmelt and rainfall during the Indian summer monsoon (Singh and Jain, 2002; Thayyen and Gergan, 2010; Bookhagen and Burbank, 2010; Andermann et al., 2012; Khan et al., 2017). However, the contribution of rainfall and snowmelt in the discharge of the Himalayan rivers vary significantly along the orogenic strike. For example, on an annual timescale, snowmelt contributes about 15-60% of discharge in the western Himalayan rivers, whereas it is less than 20% in the eastern Himalayan rivers (Bookhagen and Burbank, 2010). These rivers experience

80   a strong seasonal variability in their discharge, for instance rainfall during the Indian summer monsoon (June-September) constitutes about 60-85% of the eastern and about 50% of the annual discharge of the western Himalayan catchments.

A closer look into the hydrographs of the Himalayan rivers reveals two distinct flow regimes (Fig. 1). A clear separation of discharge during the summer monsoon and rest of the period can be observed. From May to October, most of the Himalayan rivers flow at their peak discharge due to intense and prolonged rainfall and glacier melting in the catchment; whereas, in lean

85   period (November-April), they carry relatively less discharge which remains almost constant with small fluctuations around the mean value.
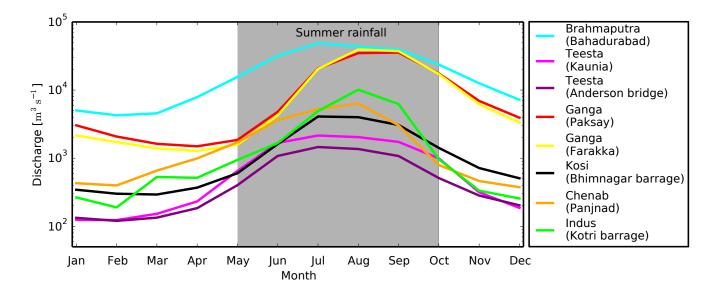
Earth **Surface**
Dynamics
Discussions

Figure 1. Hydrograph of the Himalayan Rivers

3   Morphology of alluvial river

Lacey (1930) was the first to observe a dependency of width of an alluvial river on its discharge. Based on measurements in various single-thread alluvial rivers and canals in India and Egypt, he found that the width of a river channel scales as the square root to the discharge ($e \sim 0.5$ in Eq. 1).

To explore the physical basis of Lacey's observation, Glover and Florey (1951) and Henderson (1963) developed a theory based on the concept of threshold channel. According to this theory, the balance between gravity and fluid friction maintains the sediment at threshold of motion, everywhere on the bed surface. For a given discharge (Q_w), this mechanism sets the cross-section shape and size of a channel. The resulting width (W) - discharge (Q_w) relationship reads (Seizilles, 2013; Gaurav et al., 2014; Métivier et al., 2016, 2017; Gaurav et al., 2017):

$$W = \frac{\pi}{\mu^{3/4}} \sqrt{\frac{3}{2^{3/2}\, \mathcal{K}\,[1/2]}} \, \frac{\sqrt{C_f}}{g^{1/4}} \, \frac{1}{\mathcal{L}^{1/4}} \, \sqrt{Q_w}, \tag{4}$$

where $\mathcal{L} = \theta_t \frac{(\rho_s - \rho_f) d_s}{\mu \rho_f}$ is the characteristic length (Seizilles et al., 2013), d_s is the grain size, $\rho_f \approx 1000\,\mathrm{kg\,m^{-3}}$ is the density of water and $\rho_s \approx 2650\,\mathrm{kg\,m^{-3}}$ is the density of quartz, $C_f \approx 0.1$ is the Chézy friction factor, $\theta_t \approx 0.3$ is the threshold Shields parameter, $\mu \approx 0.7$ is the Coulomb's coefficient of friction and $\mathcal{K}(1/2) \approx 1.85$ is the elliptic integral of the first kind.

Eq. 4 is the theoretical equivalent to the Lacey's law. It explains the morphology of a single thread alluvial river close to the threshold of sediment motion. In recent studies, it has been highlighted that the individual thread of the Himalayan Foreland rivers share a common regime relation (Figure. 2), and to the first order their morphology can be explained by threshold theory (Gaurav et al., 2014, 2017). Based on the measurement of width and discharge of various braided and meandering threads

in the Himalayan Foreland, they have shown that the theoretical exponent accords with the empirical exponent of the width-
105 discharge curve. However, the threads are wider than predicted by a factor of about 2 (Fig. 2). Finally they suggest that by
fitting a prefactor to the data while keeping the theoretical exponent one can establish a generalised width-discharge regime
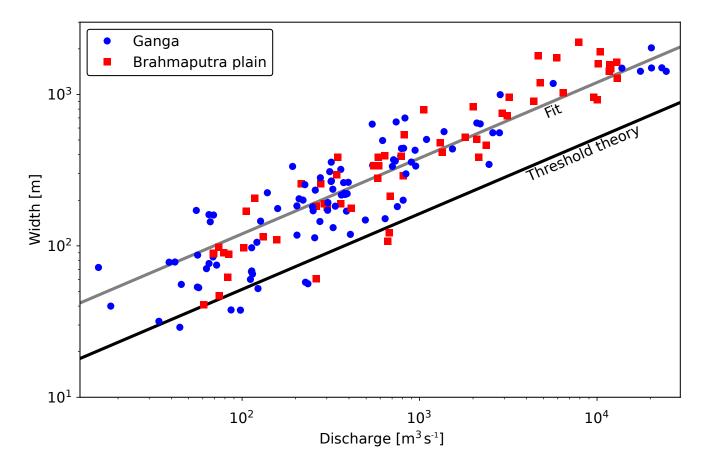relationship for the Himalayan Foreland rivers.

Figure 2. Width of the individual threads of the Himalayan Foreland rivers as a function of water discharge (after: Gaurav et al. (2017)). The
solid line (dark) is the prediction from threshold theory and the solid line (light) is obtained by fitting the prefactor of the threshold relation
(Eq.4) to the data while keeping the theoretical exponent.

4   Material and method

4.1   Dataset

110 To measure the width of a river channel, we use images acquired from Landsat Thematic Mapper (TM), Landsat 8 and Sentinel
1A satellites (Appendix A1). All images of the Landsat and Sentinel satellite missions are freely available and they can be

downloaded from the US Geological Survey (https://earthexplorer.usgs.gov) and Alaska Satellite Facility (https://www.asf.alaska.edu/sentinel) websites. We have downloaded all available cloud-free Landsat satellite images, at the locations that were near the in-situ measurement stations for which discharge data was available with us (Fig. 3). Only a few cloud free Landsat

115 images are available for the period of June to September. This is mainly because of the strong monsoon that causes intense rainfall and dense cloud covers. To overcome seasonal effect and fill the data gap during the monsoon period, we use Sentinel 1A product. Sentinel-1 satellite mission is equipped with Advanced Synthetic Aperture Radar (ASAR) sensor that operates in C-band (5.4 GHz) of microwave frequency (Schlaffer et al., 2015; Martinis et al., 2018). Advanced Synthetic Aperture Radar system can operate both day and night and has the capability to penetrate clouds and heavy rainfall. This special characteristic

120 of SAR sensors enables uninterrupted imaging of the Earth's surface during the bad weather conditions as well.

In-situ measurements of discharge for some time intervals of varying length between 1949-1975 are available for the Brahmaputra, Teesta, Ganga, Chenab, and Indus rivers of the Himalayan Foreland. They can be freely downloaded from (http://www.rivdis.sr.unh.edu/maps). We could obtain discharge data for the period 1996 - 2005, for the Ganga River at Paksay station and the Brahmaputra River at Bahadurabad station from Bangladesh. Similarly, the Ganga River discharge from 1978 -

125 2007, measured at the Farakka station in India was obtained from the Central Water Commission, Ministry of Water resources, New Delhi. We also obtained discharge data for the Kosi River for the period 2002 - 2014, from the investigation and research division, Kosi project, Birpur and from our own field measurements (Appendix A2).

4.2 Width extraction

Our main objective is to extract the width of individual river channels from satellite images. We have developed an automated

130 program in python 3.7 that takes a gray scale image as an input to classify the image pixels into binary water and non-water classes. The pixels classified as water are the foreground object and will be used to define river channels. Dry pixels serve as a background object. To extract the river channels, we use the infra-red bands of Landsat-TM and Landsat-8 images. In Landsat-TM, the infra-red ($0.76 - 0.90\,\mu\mathrm{m}$) wavelength corresponds to band 4 whereas, in Landsat-8 image, it corresponds to band 5 ($0.85 - 0.88\,\mu\mathrm{m}$). Theoretically, since water absorbs most of the infra-red radiations it appears dark, with an associated

135 brightness value close to 0. This typical characteristic of the infra-red signal allows a clear distinction between the water covered dry areas on the satellite images (Frazier et al., 2000). However, in the case of a river, the pixel intensity varies widely because of heterogeneous reflectance of river water, due to the presence of sediment and organic particles (Nykanen et al., 1998). Because the image intensity is not exactly 0 or 1, we introduce a threshold intensity to classify the pixels. Based on this criteria, we convert the gray scale image $f(x,y)$ into a binary image $g(x,y)$, which distinguished between the water-covered

140 and dry areas. This approach takes an object-background image and selects a threshold value that segments image pixels into either object (1) or background (0) (Ridler and Calvard, 1978; Sezgin et al., 2004).

$$g(x,y) = \begin{cases} 0, & \text{if } f(x,y) < T \\ 1, & \text{if } f(x,y) >= T \end{cases} \tag{5}$$
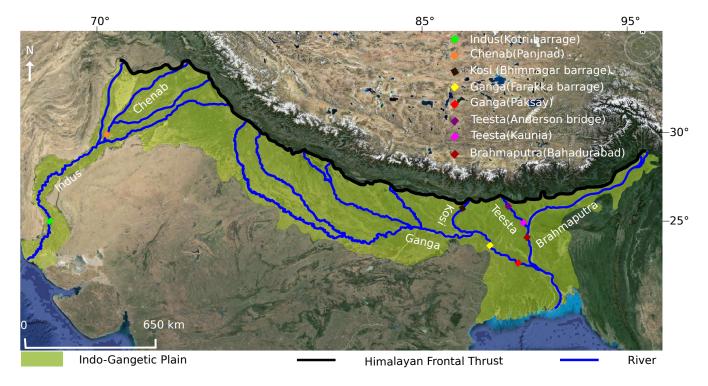
Figure 3. Location of the gauge stations of various rivers on the Indus, Ganga and Brahmaputra basins for which discharge data is available (source: https://www.google.com/earth/Google Earth).

We apply the algorithm proposed by Yanni and Horne (1994) to obtain the threshold value iteratively. Once this optimal value is obtained, we apply it to classify our pixels into water and dry classes (Fig. 4). The binary classification of satellite images into water and dry pixels can produce spurious features as well (Fig. 4). These consist of wet pixels that get classified as dry

145   or of isolated water pixels that appear randomly in the binary images (Passalacqua et al., 2013). Clusters (usually 2-3 pixels in size) that appear inside the river network do not correspond to bars or islands. We found frequent areas where strong reflection from the bed sediment cause water pixels to appear more like sand. Isolated water pixels that do not belong to the river are located in water-logged areas. We identify these types of errors and reprocess the binary images to remove them automatically.

150   For this, we first identify the isolated water patches from the binary images. To do this, we define a search window of 7×7 pixel size. We run this window on the image and look for neighboring water pixels in all surrounding directions. If a water pixel in the classified image is disconnected in all directions from the neighboring water pixels for more than seven pixels, we consider them as isolated water bodies. We therefore re-classify such pixels as dry. We re-iterate this procedure by applying a region growing algorithm (Mehnert and Jackway, 1997; Bernander et al., 2013; Fan et al., 2005). For this we initially select a water

155   seed pixel inside the river channel. The algorithm uses the initial water pixels and starts growing. This procedure removes all isolated water patches from the binary image, and retains only water pixels connected to the river network.

Earth **Surface**
Dynamics
Discussions

Raw image   Histogram   Binary image
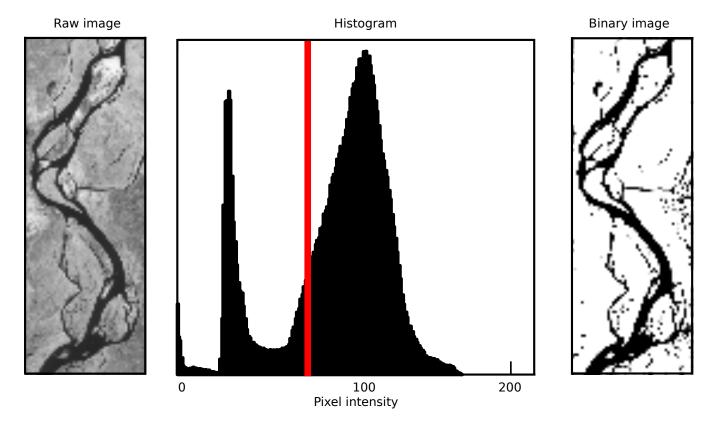

Figure 4. Histogram showing the distribution of pixel gray level intensity values. The optimal threshold (T) value (marked with red line) is obtained from the iterative threshold selection algorithm.

Once images are reclassified, we reprocess them to merge the water pixels that were initially classified as dry inside a river channel. For this we define a search window of 3×3 pixels. We choose this size by assuming that dry pixels should be more than 90 meter in size to be considered as bars or islands. Otherwise, such pixels are treated as water pixels. We move the search window on the binary image and look for neighboring dry pixels inside the river channel.

Similarly, to identify river pixels from Sentinel 1A images, we use VH (Vertical transmission and Horizontal reception) polarized band. We have Sentinel Application Platform (SNAP) v6.0 to perform the radiometric calibration, speckle noise reduction using refined Lee filter and terrain corrections and finally generate the backscatter (σ_0) image. In microwave region, open and calm water bodies exhibit low backscatter values due to high specular reflection from the water surface (Schlaffer et al., 2015; Twele et al., 2016; Amitrano et al., 2018). We manually set a threshold value to separate water and dry pixels from Sentinel-1 images. Finally, we follow a similar procedure as we developed for Landsat images to process the binary image obtained from Sentinel-1.

Once the satellite images are classified, we use the binary images to extract the width of each channel. We do this by measuring the distance from the center of a channel to its banks orthogonally to the flow direction. A detailed procedure of width extraction of a river channel is given in Appendix B.

5 Result

5.1 Accuracy assessment

To assess the precision with which we can estimate the discharge of a thread, we need to quantify the accuracy of our width-extraction procedure using Landsat and Sentinel-1 satellite images. To evaluate this, we superimpose the contours of river channels, extracted using our algorithm, to the original gray-scale images used for the extraction. We then carefully check for a match between the contours boundary and water boundary in gray scale image. We observed a good agreement between automatically extracted channel boundary and the edge of the water line in gray image. However, our algorithm fails to extract the contours of the smallest channels (60 - 90 meter in width). Several reasons explain this limitation. First, as these channels are both shallow and only a few pixels wide, their pixel intensity is close to the pixel intensity of dry areas. Therefore, the optimal threshold applied to categorize the image pixels does not identify these channels as water. Second, although an increase in the classification threshold could force the algorithm to identify these pixels as water, it would also add significant noise by classifying many dry pixels as water pixels. Such a limitation appears to be closely related to the image resolution.

Given this qualitative agreement, we proceed to evaluate the accuracy of the width extraction procedure. To do this, we overlay the transects used by the algorithm to measure the width of a thread on the original image (Fig. 5 a). We then manually measure the width at randomly selected transects for comparison. For each river, we manually measure the width at more than 15 randomly selected transects. We then compare the automatically extracted and manually measured widths.

Figure 6 compares the widths extracted automatically and manually. Most of the data points cluster on the 1:1 line. This indicates that, for the vast majority of threads, the width computed from our automated procedure is almost equal to the width measured manually.

There are some outliers however. They correspond to places along the threads where our automated procedure draws erroneous transects (Fig. 5 b). Most of such transects are located near highly curved reaches at the confluence or diffluence of two or more threads. In such places, the width of a thread is overestimated sometimes by more than 50% compared to the width measured manually. At most locations though, our procedure extracts valid transects (Fig. 5 a).

Further, we assess the distribution of relative discrepancies between automatically and manually measured widths (Fig. 7). We observe that the relative error of 90% of our measurements is centered around a mean $\mu \approx -0.02$ with a standard deviation $\sigma \approx 0.07$. This validates the width-extraction procedure.
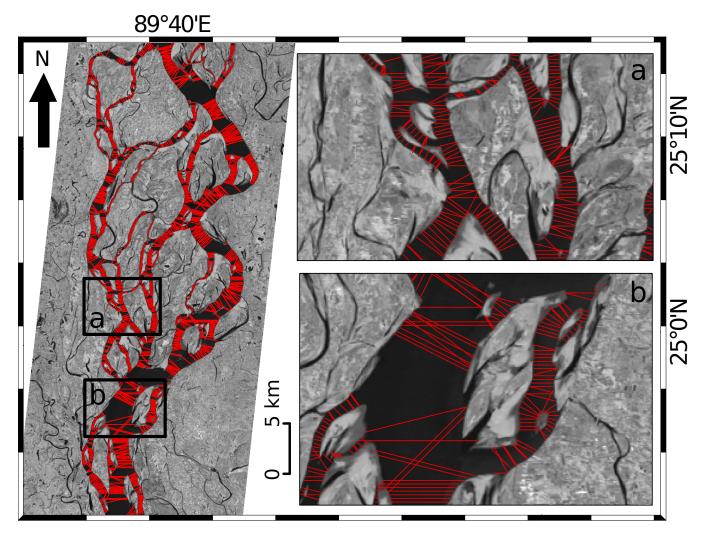
Earth **Surface**
Dynamics
Discussions

Figure 5. Width of the individual threads estimated across different transects along a reach of the Brahmaputra river from Landsat satellite image. Windows (a) and (b) illustrate the regions of valid and erroneous transects at different places in the river (image source: Landsat-TM, 29 November 2013).

5.2 Width variability along a thread

Particularly in a braided river, the width of a thread varies significantly along its course. To quantify this variability, we select a reach and plot the probability distribution of the width measured across different transects. We observed that the distribution of

200 width histograms is skewed. This skewness will be amplified in the discharge histogram because of the non-linear relationship relating the two variables. To take the skewness into account, we have used the most probable width W_m as the representative value of the width (Eq. 1).
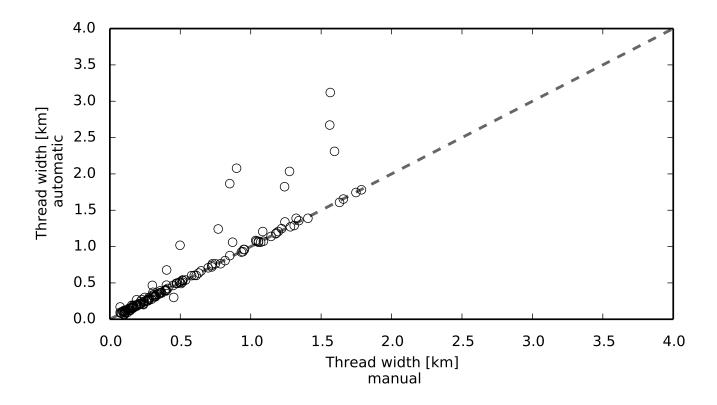
Figure 6. Threads width extracted using automated technique is plotted as function of width extracted manually.

5.3 Discharge estimation

We now proceed to estimate discharge (Q_w) for the Himalayan Rivers based on their channel widths measured from satellite

205 images. To have a meaningful comparison between the image derived discharge and the corresponding in-situ measurement, we select a reach about ten times longer than the width of a river on satellite images. In the case of a braided river, we consider the widest channel to define reach length. In the selected reach we assume that discharge is conserved, there is no significant addition or extraction of water in the river.

To estimate discharge of the study reach, we use a regime relation established by Gaurav et al. (2017) based on threshold

210 channel theory (Eq. 4) and field measurements of channel's width and discharge on the Ganga-Brahmaputra Plain. The resulting regime relation is governed by:

$$Q_w = \left(\frac{W_m}{\alpha}\right)^2 \sqrt{gd_s}, \tag{6}$$

where α is the best-fit coefficient, an empirical value obtained from fitting the prefactor of the regime curve (Eq.4) and W_m is the most probable width.
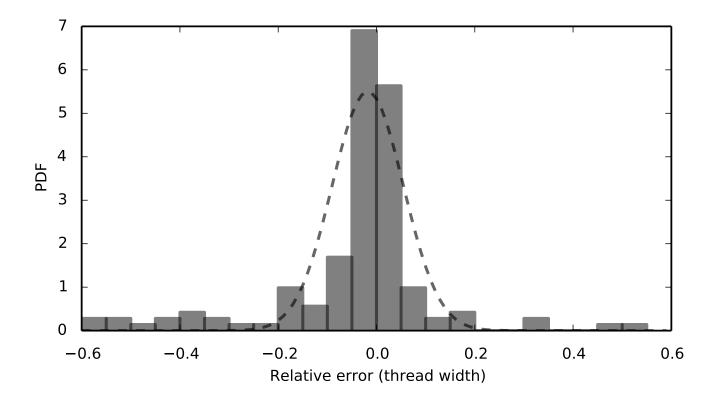
Figure 7. Distribution of the error in the threads width extracted automatically. The corresponding normal distribution is obtained by removing the 10% extreme values from the distribution.

We use Eq. 6 to calculate the discharge for threads of known width. Because the river width scales non-linearly with discharge, regime relations obtained refer to the total width in the case of a braided river; and will not be the same as those obtained for individual threads. Since most of the studied rivers are braided, we first calculate the discharge for individual threads across a given section. We then sum the discharge of the individual threads across a transect to compute the total discharge at a section.

5.4 Estimated Vs. measured discharge

Once monthly discharges for all the rivers are estimated from satellite images, we compare them with the average monthly discharge measured at the corresponding gauge stations. To do so, we plot the hydrographs of the estimated and measured discharges together (Fig. 8). We observe that the estimated discharge from satellite images remains constant throughout the year, except during the monsoon period (June-September) when all the rivers show a significant rise. During the non-monsoon period (October-May), estimated discharges for most of our rivers are overestimated. To the first order, our approach is able to capture the rising trend of discharges during the monsoon period, however the estimated discharges are lesser than the measured discharges. Table 2 compares the estimated and measured discharges during the monsoon period. For most of our

rivers, the difference between measured and estimated discharges are less than $50\,\%$; though this difference is comparatively high for the Indus ($72 - 78\,\%$) and Chenab ($36 - 67\,\%$) rivers (Table 2).
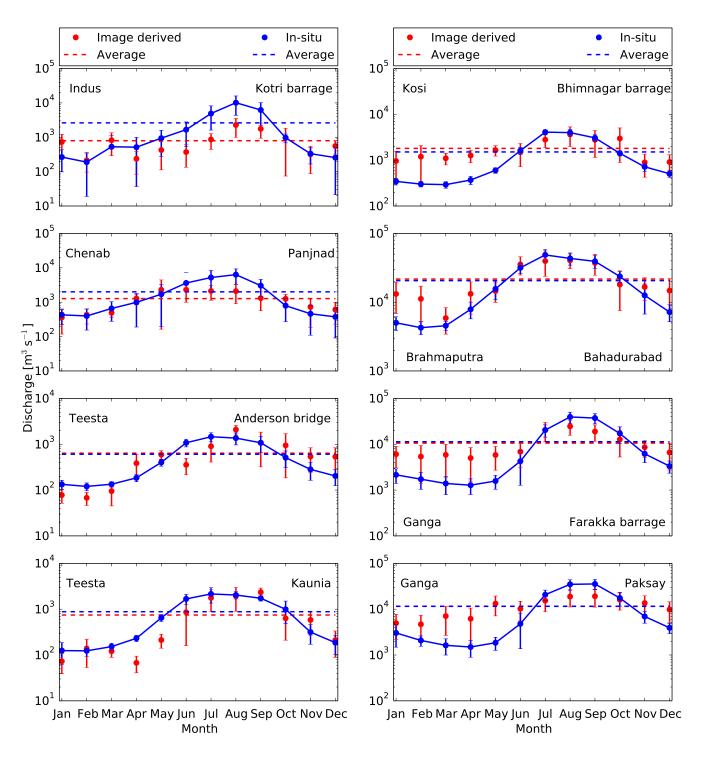
Figure 8. Hydrograph of satellite derived river discharge against their monthly average discharge recorded at the gauging station. Dotted red and blue lines are the annual average discharge obtained from satellite images and in-situ measurement respectively.

	Monsoon discharge $[m^3 s^{-1}]$			
Rivers	Jun	Jul	Aug	Sept
Kosi (Bhimnagar barrage)				
In-situ	1616 ± 285	4091 ± 530	3998 ± 660	3072 ± 509
Image derived	1515 ± 797	2800 ± 912	3660 ± 1667	2796 ± 1644
Difference (%)	-6	-32	-8	-9
Brahmaputra (Bahadurabad)				
In-situ	31717 ± 5536	48769 ± 9640	43387 ± 8722	39320 ± 8071
Image derived	35335 ± 10491	39716 ± 15914	40653 ± 9808	37316 ± 12580
Difference (%)	11	-19	-6	-5
Ganga (Farakka barrage)				
In-situ	4260 ± 2989	20375 ± 6059	39462 ± 10665	37264 ± 9415
Image derived	6864 ± 3717	20599 ± 9343	24562 ± 8871	18971 ± 7364
Difference (%)	61	1	-38	-49
Ganga (Paksay)				
In-situ	4794 ± 3425	20691 ± 5427	34887 ± 9002	35546 ± 8985
Image derived	10226 ± 4689	15333 ± 6510	18862 ± 7691	19168 ± 8089
Difference	113	-26	-46	-46
Teesta (Anderson bridge)				
In-situ	1078 ± 204	1458 ± 330	1363 ± 395	1076 ± 416
Image derived	356 ± 139	904 ± 494	2086 ± 494	1079 ± 759
Difference (%)	-67	-38	53	0
Teesta (Kaunia)				
In-situ	1674 ± 428	2151 ± 792	2037 ± 369	1733 ± 227
Image derived	860 ± 700	1765 ± 883	1938 ± 1036	2346 ± 540
Difference (%)	-49	-18	-5	35
Indus (Kotri barrage)				
In-situ	1665 ± 1136	4912 ± 3290	10128 ± 5807	6227 ± 3980
Image derived	372 ± 238	861 ± 417	2279 ± 1279	1759 ± 826
Difference (%)	-78	-82	-77	-72
Chenab (Panjnad)				
In-situ	3621 ± 2812	5235 ± 3206	6340 ± 2983	3038 ± 1574
Image derived	2300 ± 1302	2125 ± 988	2099 ± 1193	1311 ± 749
Difference (%)	-36	-59	-67	-57

Table 1. Comparison between the image derived and in-situ measured discharge of the Himalayan rivers during the Indian summer monsoon period.

6 Discussion

230 It is important to note that the discharge estimated from satellite images does not correspond to an instantaneous discharge. To understand the emergence of constant hydrograph from the estimated discharge derived from satellite images we explore the concept of channel forming (formative) discharge i.e. a discharge that sets the geometry of alluvial river channels. Several workers Inglis and Lacey (1947); Leopold and Maddock (1953); Blench (1957), have shown that the geometry of an alluvial channel corresponds to a formative discharge (see table A3 in appendix for the definition of different discharges). They have

235 discussed how a limited range of flows are responsible for shaping its channel. At low-flow discharge, the water simply flows through the threads without affecting their geometry. Schumm and Lichty (1965) used the concept of time span (geologic, modern and present) in defining the interrelationship between dependent and independent variables of a river system. According to them, morphology of a river channel is set in the modern time span (last 1000 years) by the average discharge of water and sediment. In the present time span (1 year or less), channel morphology can be considered as independent variable against

240 instantaneous discharge of water and sediment.

Similarly, it has been argued by Inglis and Lacey (1947); Leopold and Maddock (1953); Blench (1957) that it is not the highest flows that contribute the most in shaping a river channel. Such high discharges are capable of transforming the channel, but they occur so infrequently that, on average, their morphological impact is small. Wolman and Miller (1960) highlighted that the bankfull discharge that occurs once each year or every two years sets the pattern and channel width of the alluvial rivers.

245 Formative discharge for the Himalayan rivers is expected to occur in the monsoon period, thus one may expect that during low flow such rivers maintain their flows without modifying the existing channel geometry. This is probably why our estimated discharge from satellite images remain constant throughout and is mostly overestimated than the measured discharge at gauge stations.

According to Inglis and Lacey (1947), rivers approach their equilibrium geometry for a formative discharge that approxi-

250 mately corresponds to the bankfull discharge. They suggested this discharge lies between 1/2 and 2/3 of the maximum discharge. It has also been suggested that the formative discharge corresponds to the median discharge (Blench, 1957). In their study, Leopold and Maddock (1953) used the discharge that corresponds to a given frequency of occurrence and compared it to the hydraulic geometry of the river. Based on their observations in the United States, they recommended the use of the annual average discharge as a proxy for the formative discharge. Hereafter, we use the definition of Leopold and Maddock (1953).

255 Based on our understanding of the geometry of alluvial river channels, we argue that the width of the thread that we extract from satellite images corresponds to a formative discharge. Therefore for a given river, discharge estimated from these widths should compare with the formative discharge. We now evaluate how the discharge estimated from satellite data varies with time. We plot the monthly discharge estimated for all of our rivers to their corresponding average monthly discharge measured at the gauge stations (Fig. 8). As suggested earlier by Inglis and Lacey (1947); Leopold and Maddock (1953) and Blench (1957) we

260 observe that the estimated discharges from images are nearly constant throughout the year, with only small fluctuations around their mean. This supports the hypothesis that the width of the thread extracted from satellite images corresponds to a formative discharge.

Now we compare the discharge estimated from satellite images to the discharge measured at a nearby gauging station. To do this, we first compare the annual average discharge estimated from Landsat and Sentinel-1A images for different months to

265   the annual average discharge measured at corresponding ground stations. We plot these discharges on a log-log scale (Fig. 9). The discharge estimated from satellite images agrees to an order of magnitude with the measured discharge.
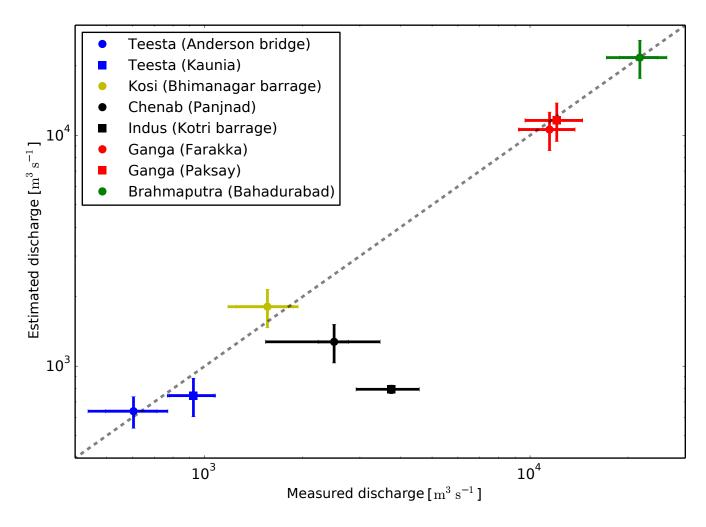

Figure 9. Satellite-derived river discharge against annual average discharge measured at a ground station. Error bar in measured discharge represent the standard deviation. Error bar for estimated discharge is calculated by considering $\pm 10\%$ measurement uncertainty in the channels width from satellite images.

The difference between measured and estimated annual average discharges for the Brahmaputra, Ganga, Kosi, and Teesta rivers is less than 20%. However, this difference is comparatively high for the Indus (78%) and Chenab (49%) rivers. Interestingly, the estimated discharge for the Teesta (at Anderson station), Ganga (at Farakka & Paksay) and Brahmaputra (at

270   Bahadurabad) rivers converge to their measured discharge with a small difference of 5%, 8%, 4% and $< 1\%$, respectively

(table 2); whereas the estimated discharge of the Teesta (at Kaunia station) and Kosi (at Bhimnagar) show a relatively higher difference of 19%, and 16%. This difference could be possibly related to the anthropogenic impact on the natural flow condition. For example, the selected study reaches for the Teesta (at Kaunia station) and Kosi (at Bhimnagar) rivers is located near the barrage where flow is highly regulated. However, this relationship is not entirely clear at this stage.

275   Similarly, the large difference between the estimated and measured discharge of the Indus and Chenab rivers could possibly be related to a series of dams and barrages (Kotri barrage, 1955, Mangla dam, 1967, Tarbela dam, 1976) that have been constructed. Such interventions have significantly altered the water and sediment discharge of the Indus river. For example, downstream of the Kotri barrage, the average annual water discharge of the Indus river has declined at an alarming rate of about $(107 \text{ to } 10) \times 10^9 \, \text{m}^3$ from 1954 to 2003 (Inam et al., 2007). This continuous decline in the average annual discharge might

280   have significantly modified the geometry of the Indus river.

River	Station	$\langle Q_{insitu} \rangle$ m^3s^{-1}	$\langle Q_{sat.} \rangle$ m^3s^{-1}	$Q_{diff.}$ m^3s^{-1}	$Q_{diff.}$ $\%$
Teesta	Anderson	605 ± 109	638 ± 165	33	5
Teesta	Kaunia	924 ± 144	745 ± 155	-179	19
Kosi	Bhimnagar	1559 ± 313	1810 ± 380	251	16
Chenab	Panjnad	2500 ± 961	1275 ± 268	-1225	49
Indus	Kotri	3745 ± 825	794 ± 162	-2951	78
Ganga	Farakka	11477 ± 2279	10593 ± 2225	-884	8
Ganga	Paksay	12080 ± 2403	11605 ± 2438	-475	4
Brahmaputra	Bahadurabad	21751 ± 2942	21717 ± 4740	-34	< 1

Table 2. Annual average discharge estimated from satellite images and corresponding gauging stations.

7   Conclusion and future outlook

The semi-empirical regime relation established by Gaurav et al. (2017) and remote sensing images can be used to obtain a first order estimate of the formative discharge of any river in the Himalayan Foreland. The regime equation used here is based on threshold theory and instantaneous measurements in various braided and meandering rivers. These measurements were

285   acquired during the period when rivers of the Himalayan Foreland usually flow at their formative discharge. Therefore, this regime equation only provides an estimate of the formative discharge, and it can not capture the instantaneous variations of discharge. On the other hand, as this regime relation is established from the measurements in braided and meandering rivers, it can be used to estimate the discharge in a river of any planform. It is especially useful and relevant for braided rivers that present several difficulties for the measurement of discharge in the field. As this regime equation is generalized and independent

290   of any specific location, it can be used to estimate discharge at any location by just measuring the channel width on satellite or aerial images.

Using this semi-empirical regime equation and satellite images of Landsat and sentinel-1 missions, we have estimated the discharge of six major rivers in the Himalayan Foreland (Brahmaputra, Chenab, Ganga, Indus, Kosi, and Teesta). Our estimated discharges compare with the average annual discharge measured at the nearest gauging stations. This first-order agreement al-
295 though encouraging, requires further research to improve the degree of agreement between measured and estimated discharges. Better resolution remote sensing images would most likely improve the agreement between estimated and in-situ discharge. Several reasons may explain the observed uncertainties and call for future work.

This study is a step towards obtaining first order estimates of discharge in ungauged river basins solely from satellite image derived data. It can be used for the sustainable river development and management to ensure regional water security, especially
300 in the regions where river discharge is not readily available.

Appendix A: Dataset

A1   Satellite images

Detailed specification of satellite data (Landsat and Sentinel-1) used in this study. Table A1

Landsat-TM & Landsat-8				
River	**Date**	**Scene ID**	**Satellite**	**Gauge station**
Brahmaputra	2009-01-18	LT51380432009018KHC01	L-TM	15.18/89.66
Brahmaputra	2009-02-19	LT51380432009050KHC00	L-TM	15.18/89.66
Brahmaputra	2014-03-21	LC81380432014080LGN00	L-8	15.18/89.66
Brahmaputra	2014-04-22	LC81380432014112LGN00	L-8	15.18/89.66
Brahmaputra	2014-10-31	LC81380432014304LGN00	L-8	15.18/89.66
Brahmaputra	2013-11-29	LC81380432013333LGN00	L-8	15.18/89.66
Brahmaputra	2014-12-02	LC81380432014336LGN00	L-8	15.18/89.66
Chenab	2014-01-04	LC81500402014004LGN00	L-8	29.34/71.02
Chenab	2018-02-16	LC81500402018047LGN00	L-8	29.34/71.02
Chenab	2015-04-13	LC81500402015103LGN00	L-8	29.34/71.02
Chenab	2014-05-28	LC81500402014148LGN00	L-8	29.34/71.02
Chenab	2014-06-29	LC81500402014180LGN00	L-8	29.34/71.02
Chenab	2014-07-15	LC81500402014196LGN00	L-8	29.34/71.02
Chenab	2014-10-19	LC81500402014292LGN00	L-8	29.34/71.02
Chenab	2013-11-01	LC81500402013305LGN00	L-8	29.34/71.02
Chenab	2014-12-06	LC81500402014340LGN00	L-8	29.34/71.02
Ganga	2015-02-11	LC81390432015042LGN01	L-8	24.83/87.92
Ganga	2015-03-15	LC81390432015074LGN00	L-8	24.83/87.92

Ganga	2013-04-02	LT51390432010092KHC00	L-8	24.83/87.92
Ganga	2014-06-16	LC81390432014167LGN00	L-8	24.83/87.92
Ganga	2014-11-23	LC81390432014327LGN00	L-8	24.83/87.92
Ganga	2009-01-18	LT51380432009018KHC01	L-TM	24.08/89.03
Ganga	2009-02-19	LT51380432009050KHC00	L-TM	24.08/89.03
Ganga	2014-03-21	LC81380432014080LGN00	L-8	24.08/89.03
Ganga	2014-04-22	LC81380432014112LGN00	L-8	24.08/89.03
Ganga	2014-10-31	LC81380432014304LGN00	L-8	24.08/89.03
Ganga	2013-11-29	LC81380432013333LGN00	L-8	24.08/89.03
Ganga	2014-12-02	LC81380432014336LGN00	L-8	24.08/89.03
Indus	2015-01-05	LC81520422015005LGN00	L-8	25.35/66.35
Indus	2017-02-11	LC81520422017042LGN00	L-8	25.35/66.35
Indus	2015-03-10	LC81520422015069LGN00	L-8	25.35/66.35
Indus	2014-04-24	LC81520422014114LGN00	L-8	25.35/66.35
Indus	2014-06-27	LC81520422014178LGN00	L-8	25.35/66.35
Indus	2014-10-17	LC81520422014290LGN00	L-8	25.35/66.35
Indus	2014-11-18	LC81520422014162LGN00	L-8	25.35/66.35
Kosi	1991-01-15	LT51400421991015ISP00	L-TM	26.52/86.92
Kosi	2011-02-07	LT51400422011038BKT00	L-TM	26.52/86.92
Kosi	1992-03-06	LT51400421992066ISP00	L-TM	26.52/86.92
Kosi	2018-05-01	LC81400422018121LGN00	L-8	26.52/86.92
Kosi	2015-09-30	LC81400422015273LGN01	L-8	26.52/86.92
Kosi	2000-10-14	LE71400422000288SGS00	L-TM	26.52/86.92
Kosi	2013-11-11	LC81400422013315LGN00	L-TM	26.52/86.92
Kosi	2002-12-07	LE71400422002341SGS00	L-TM	26.52/86.92
Teesta	2014-04-22	LC81380422014112LGN00	L-8	26.33/88.87
Teesta	2014-10-31	LC81380422014304LGN00	L-8	26.33/88.87
Teesta	2014-11-16	LC81380422014320LGN00	L-8	26.33/88.87
Teesta	2014-12-02	LC81380422014336LGN00	L-8	26.33/88.87
Teesta	2015-03-08	LC81380422015067LGN00	L-8	25.70/89.50
Teesta	2014-04-22	LC81380422014112LGN00	L-8	25.70/89.50
Teesta	2014-10-31	LC81380422014304LGN00	L-8	25.70/89.50
Teesta	2014-12-02	LC81380422014336LGN00	L-8	25.70/89.50
Sentinel-1A				
Ganga	2017-10-17	S1A_IW_GRDH ⋯ _31A9_Cal_Spk_TC	S-1A	24.83/87.92

Earth **Surface**
Dynamics
Discussions

EGU

Ganga	2018-07-20	S1A_IW_GRDH ⋯	_BE68_Cal_Spk_TC	S-1A	24.83/87.92
Ganga	2018-05-18	S1A_IW_GRDH ⋯	_114F_Cal_Spk_TC	S-1A	24.83/87.92
Ganga	2018-08-10	S1A_IW_GRDH ⋯	_6C38_Cal_Spk_TC	S-1A	24.83/87.92
Ganga	2018-09-06	S1A_IW_GRDH ⋯	_4CBB_Cal_Spk_TC	S-1A	24.83/87.92
Ganga	2016-04-13	S1A_IW_GRDH ⋯	_4BF4_Cal_Spk_TC	S-1A	24.83/87.92
Ganga	2018-01-18	S1A_IW_GRDH ⋯	_831D_Cal_Spk_TC	S-1A	24.83/87.92
Ganga	2017-09-27	S1A_IW_GRDH ⋯	_2DC4_Cal_Spk_TC	S-1A	24.08/89.03
Ganga	2018-05-13	S1A_IW_GRDH ⋯	_EF71_Cal_Spk_TC	S-1A	24.08/89.03
Ganga	2018-06-08	S1A_IW_GRDH ⋯	_035D_Cal_Spk_TC	S-1A	24.08/89.03
Ganga	2018-07-12	S1A_IW_GRDH ⋯	_8CBA_Cal_Spk_TC	S-1A	24.08/89.03
Ganga	2018-08-17	S1A_IW_GRDH ⋯	_EF93_Cal_Spk_TC	S-1A	24.08/89.03
Brahamputra	2018-07-14	S1A_IW_GRDH ⋯	_2752_Cal_Spk_TC	S-1A	15.18/89.66
Brahamputra	2017-11-14	S1A_IW_GRDH ⋯	_BA85_TC_Cal	S-1A	15.18/89.66
Brahamputra	2018-05-15	S1A_IW_GRDH ⋯	_9533_Cal_Spk_TC	S-1A	15.18/89.66
Brahamputra	2017-09-17	S1A_IW_GRDH ⋯	_E022_Cal_Spk_TC	S-1A	15.18/89.66
Brahamputra	2018-06-18	S1A_IW_GRDH ⋯	_8D0F_Cal_Spk_TC	S-1A	15.18/89.66
Brahamputra	2018-08-19	S1A_IW_GRDH ⋯	_173D_Cal_Spk_TC	S-1A	15.18/89.66
Chenab	2018-09-07	S1A_IW_GRDH ⋯	_3240_Cal_Spk_TC	S-1A	29.34/71.02
Chenab	2018-08-14	S1A_IW_GRDH ⋯	_A3CB_Cal_Spk_TC	S-1A	29.34/71.02
Chenab	2018-03-19	S1A_IW_GRDH ⋯	_2E5E_Spk_TC	S-1A	29.34/71.02
Chenab	2018-02-23	S1A_IW_GRDH ⋯	_741E_TC_Cal_Spk	S-1A	29.34/71.02
Indus	2018-07-10	S1A_IW_GRDH ⋯	_4B89_Cal_Spk_TC	S-1A	25.35/66.35
Indus	2018-05-11	S1A_IW_GRDH ⋯	_CE83_Cal_Spk_TC	S-1A	25.35/66.35
Indus	2017-09-13	S1A_IW_GRDH ⋯	_7DD5_Cal_Spk_TC	S-1A	25.35/66.35
Indus	2018-08-27	S1A_IW_GRDH ⋯	_DA34_Cal_Spk_TC	S-1A	25.35/66.35
Teesta	2017-09-03	S1A_IW_GRDH ⋯	_32D8_Cal_Spk_T	S-1A	25.70/89.50
Teesta	2018-01-13	S1A_IW_GRDH ⋯	_022569	S-1A	25.70/89.50
Teesta	2018-05-13	S1A_IW_GRDH ⋯	_021886	S-1A	25.70/89.50
Teesta	2018-06-06	S1A_IW_GRDH ⋯	_022236	S-1A	25.70/89.50
Teesta	2018-07-12	S1A_IW_GRDH ⋯	_022761	S-1A	25.70/89.50
Teesta	2018-08-29	S1A_IW_GRDH ⋯	_023461	S-1A	25.70/89.50
Teesta	2017-09-03	S1A_IW_GRDH ⋯	_32D8_Cal_Spk_TC	S-1A	26.33/88.87
Teesta	2018-01-13	S1A_IW_GRDH ⋯	_50B1_Cal_Spk_TC	S-1A	26.33/88.87
Teesta	2018-05-13	S1A_IW_GRDH ⋯	_D8D7_Cal_Spk_TC	S-1A	26.33/88.87
Teesta	2018-06-06	S1A_IW_GRDH ⋯	_1753_Cal_Cal_TC	S-1A	26.33/88.87

Earth **Surface**
Dynamics
Discussions

Teesta	2018-07-12	S1A_IW_GRDH ⋯ _F499_Cal_Spk_TC	S-1A	26.33/88.87
Teesta	2018-08-29	S1A_IW_GRDH ⋯ _341E_Cal_Spk_TC	S-1A	26.33/88.87
Kosi	2018-08-18	S1A_IW_GRDH ⋯ _8CB2_Cal_Spk_TC	S-1A	26.52/86.92
Kosi	2018-06-19	S1A_IW_GRDH ⋯ _9B41_Cal_Spk_TC	S-1A	26.52/86.92
Kosi	2017-04-25	S1A_IW_GRDH ⋯ _32C5_Cal_Spk_TC	S-1A	26.52/86.92
Kosi	2017-07-30	S1A_IW_GRDH ⋯ _2658_Cal_Spk_TC	S-1A	26.52/86.92

Table A1 Details of the Landsat-8 (L-8), Landsat-TM (L-TM) and Sentinel-1A (S-1A) satellite images used in this study. Gauge station is the location (lat/lon) of nearest in-situ discharge measurement stations.

A2   Description of satellite and in-situ dataset

305   Table A2 contains a detailed description of in-situ discharge data for different rivers used in this study. This includes, data source, location of gauge station and period of measurement.

In-situ data (discharge)					
River	Station	location		Period	Source
		Longitude (degree)	Latitude (degree)		
Teesta	Anderson	88.87	26.33	1965-1971	RivDIS
	Kaunia	89.50	25.70	1969-1975	RivDIS
Kosi	Bhimnagar	86.92	26.52	2002-2014	Kosi barrage Birpur
Chenab	Panjnad	71.30	29.35	1973-1979	RivDIS
Indus	Kotri	68.35	25.35	1973-1979	RivDIS
Ganga	Farakka	87.92	24.83	1949-1973 1978-2007	RivDIS & CWC
	Paksay	89.03	24.08	1965-1975 1996-2005	RivDIS & Dhaka Univ.
Brahmaputra	Bahadurabad	89.66	25.18	1969-1975 1996-2005	RivDIS & Dhaka Univ.

Table A2. Satellite images used for the extraction of channels width. In-situ discharge data is freely available and were downloaded from (http://www.rivdis.sr.unh.edu/maps/asi/).

Type	Defination	Remarks	Source
Instantaneous discharge	discharge at any given time in space	usually measured at gauge stations installed on rivers	Chow (2010), Navratil et al. (2006)
Monthly average discharge	average discharge in a given month of the year	calculated by taking the mean of each month for the entire period of record	Chow (2010)
Annual average discharge	average discharge in a given year or time series	calculated by taking the mean of total discharge in a year or period	Chow (2010)
Median discharge	median value of discharge in a given year or period	calculated by finding the median value from the discharge time series of a given period	Blench (1957)
Bankfull discharge	discharge that completely fills the channel.	occurs once every year or in every two years	Wolman and Miller (1960), Navratil et al. (2006) (Rhoads, 2020, p. 145)
Formative discharge	derived discharge that would result in the same hydraulic geometry as the long-term hydrograph.	corresponds to average annual discharge, median flood discharge, and bankfull discharge	Leopold and Maddock (1953), Wolman and Miller (1960), Bolla Pittaluga et al. (2014) (Rhoads, 2020, p. 144)

Table A3. A summary of terminology used for different discharges in this study.

A3 Glossary

Appendix B: Satellite image processing

B0.1 Identification of river channels

310 To identify the river and non river pixels, we have used the infra-red bands of Landsat-TM and Landsat-8 images. In Landsat-TM, the infra-red $(0.76 - 0.90 \mu m)$ wavelength corresponds to band 4 whereas, in Landsat-8 image, it corresponds to band 5 $(0.85 - 0.88 \mu m)$.

We obtained an optimal threshold value by using the algorithm initially proposed by Yanni and Horne (1994). We than used the optimal threshold value to separate water and dry pixels from Landsat satellite images. The algorithm initiate by

315 selecting a threshold as a midpoint value that lies in between the maximum and minimum gray level intensity (gi) as $gi_{mid} = (gi_{max} + gi_{min})/2$, where gi_{max} is the highest and gi_{min} is the lowest gray level intensity. Based on this initial threshold, the image pixels are clustered into foreground and background objects. After each iteration the threshold value is updated using the mean intensity of both the clusters. Finally the algorithm terminates when the threshold converges.

B0.2   Removal of artefacts

320   Thresholding a gray scale input satellite image into binary class (water and dry pixels) produces spurious features. These consist of wet pixels that get classified as dry or of isolated water pixels that appear randomly in the binary images. Clusters (usually 2-3 pixels in size) that appear inside the river network do not corresponds to bars or islands. They appear to be more frequent in the areas where strong reflection from the bed sediment cause water pixels to appear more like a sand. Isolated water pixels that do not belong to the river are disconnected and located in water-logged areas. We have identified both of

325   these type errors from binary image and reprocess to remove them automatically. While doing this we first define a seed point inside the main channel and run the flood filling algorithm (Mehnert and Jackway, 1997; Bernander et al., 2013; Fan et al., 2005). This identify water pixels in a river channel those are connected and remove the isolated water pixels those have poor connectivity (Fig. B1).
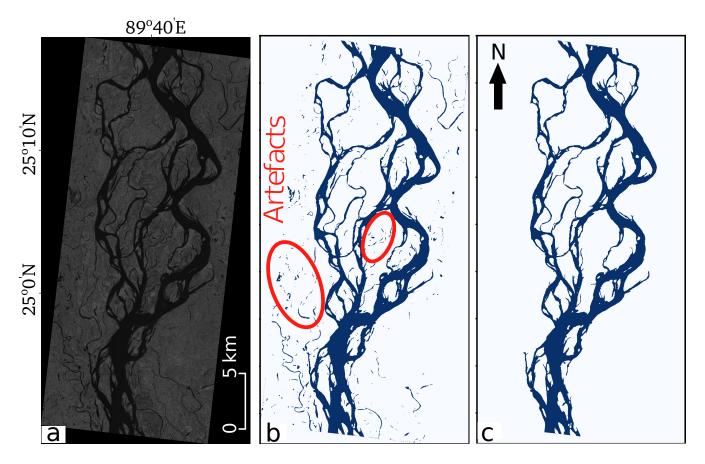

Figure B1. (a) Input Landsat-8 image of short wave infra-red wavelength is threshold to create binary image having water (blue) and dry (white) pixels. (b) Binary image with isolated water patches and artefacts and (c) removed artefacts (image source: Landsat-TM, 29 November 2013).

B0.3 Extraction of channel's skeleton and contour

330 Our channel width extraction algorithm requires to river's centerline and boundary. A river centerline often called skeleton in computer vision corresponds to its median axis. To identify the river skeleton, we have used a thinning algorithm to extract river's centerline. The algorithm iteratively reduces the boundary pixels in a way that preserves its topology (for example eroding pixels must not alter the geometric properties of the object studied) and connectivity (Fig. B2 a). The final skeleton is centered within the object and reflects its geometrical properties (Zhang and Suen, 1984; Baruch, 1988; Lam et al., 1992;

335 Chatbri et al., 2015). The thinning algorithms produces several small centre line segments, often less than 300 meter in length, that are disconnected from the channel network at one end. These segments of the skeleton are too small to be considered as part of the river network. For our purpose we consider such segments as noise and filter them out. We do this iteratively, by looking for skeleton segments those are disconnected from the skeleton network at one end.

To extract the channel banks, we have applied a contour extraction algorithm that detects the outer boundary of a channel

340 (Fig. B2). The algorithm relies on a pixel-neighbourhood analysis, where a pixel in a binary image is considered a contour pixel, if it has at least one background neighbour (Chatbri et al., 2015).

B0.4 Channel's width calculation

Once the satellite images are processed to extract skeleton and channel's banks, we then proceed to extract the width of each channels. We do this by measuring the distance from the centre of a channel to its banks orthogonally to the flow. From the

345 skeleton of the image we draw a perpendicular line to the river bank and measure the the euclidean distance (Fig. B3). In case of a braided river, especially near the junctions where more than two river join or bifurcate form a complex network. At such locations our algorithm fails to measure correct width. To circumvent this we identify all the junctions from river skeleton (Fig. B2b). In the proximity of junction we consider an area of 5 pixels and define them as a zone of channel's confluence and diffluence. In this zone we avoid to calculate the width of the channels.

350 Finally, we draw perpendicular transects from each pixel of the skeleton to both side of the channel and calculate the distance from any point (x, y) on the skeleton to its corresponding left (x_1, y_1) and right (x_2, y_2) points on the channel boundary (Fig. B3). We then sum these widths to get the total width across a transect. For simplicity, at every one kilometer distance along the channel we compute the most probable width of each channels across a river section. Finally, the discharges through a section can be calculated along an entire reach (Fig. B3).
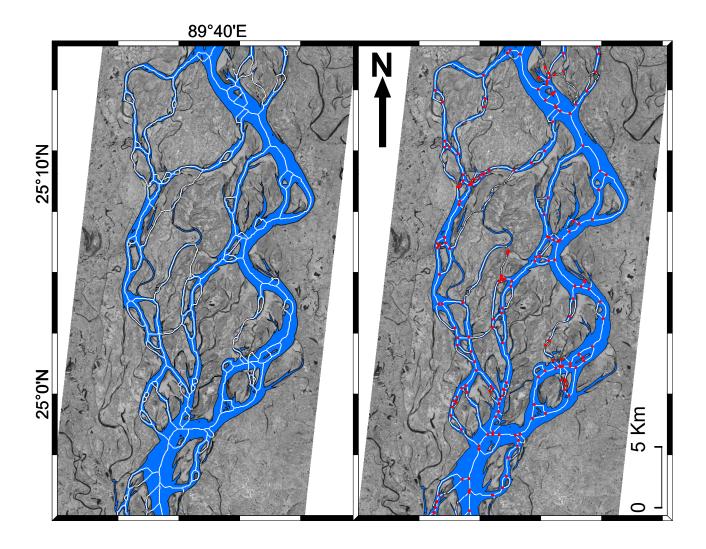
Figure B2. In left: river center line (skeleton) and boundary (contour) are superimposed on Landsat-8 satellite image. In right: image illustrates the stream junction identified on skeleton (image source: Landsat-TM, 29 November 2013).

Competing interests. The authors declare that they have no conflict of interest
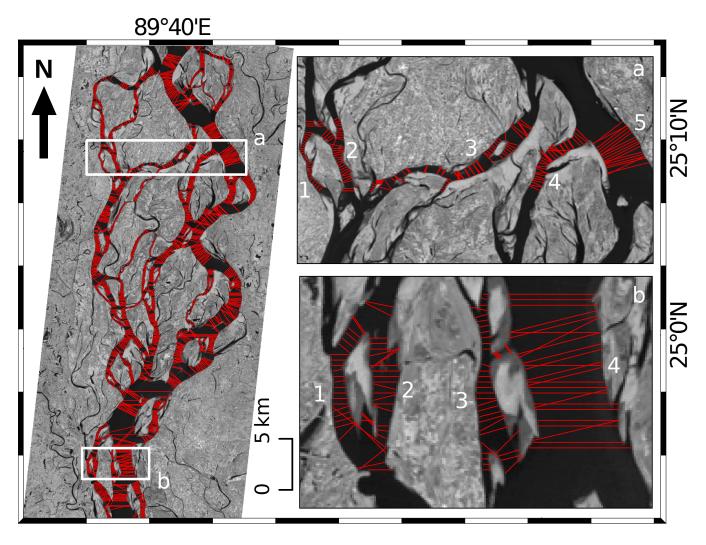
Figure B3. Width extracted across each of the individual channels. Image in the right illustrates the reach lengths (in boxes) over which most probable width of each channels is calculated (image source: Landsat-TM, 29 November 2013).

References

365

Allen, G. H. and Pavelsky, T. M.: Global extent of rivers and streams, Science, 361, 585–588, 2018.

Alsdorf, D. E., Melack, J. M., Dunne, T., Mertes, L. A., Hess, L. L., and Smith, L. C.: Interferometric radar measurements of water level changes on the Amazon flood plain, Nature, 404, 174–177, 2000.

Alsdorf, D. E., Rodríguez, E., and Lettenmaier, D. P.: Measuring surface water from space, Reviews of Geophysics, 45, 2007.

370 Amitrano, D., Di Martino, G., Iodice, A., Riccio, D., and Ruello, G.: Unsupervised Rapid Flood Mapping Using Sentinel-1 GRD SAR Images, IEEE Transactions on Geoscience and Remote Sensing, 56, 3290–3299, 2018.

Andermann, C., Longuevergne, L., Bonnet, S., Crave, A., Davy, P., and Gloaguen, R.: Impact of transient groundwater storage on the discharge of Himalayan rivers, Nature Geoscience, 5, ngeo1356, 2012.

Andreadis, K. M., Clark, E. A., Lettenmaier, D. P., and Alsdorf, D. E.: Prospects for river discharge and depth estimation through assimilation
375 of swath-altimetry into a raster-based hydrodynamics model, Geophysical Research Letters, 34, 2007.

Ashmore, P. and Sauks, E.: Prediction of discharge from water surface width in a braided river with implications for at-a-station hydraulic geometry, Water Resources Research, 42, 2006.

Baruch, O.: Line thinning by line following, Pattern Recognition Letters, 8, 271–276, 1988.

Bernander, K. B., Gustavsson, K., Selig, B., Sintorn, I.-M., and Hendriks, C. L. L.: Improving the stochastic watershed, Pattern Recognition
380 Letters, 34, 993–1000, 2013.

Bjerklie, D. M., Moller, D., Smith, L. C., and Dingman, S. L.: Estimating discharge in rivers using remotely sensed hydraulic information, Journal of Hydrology, 309, 191–209, 2005.

Blench, T.: Regime behaviour of canals and rivers, Butterworths Scientific Publications London, 1957.

Bolla Pittaluga, M., Luchi, R., and Seminara, G.: On the equilibrium profile of river beds, Journal of Geophysical Research: Earth Surface,
385 119, 317–332, 2014.

Bookhagen, B. and Burbank, D. W.: Toward a complete Himalayan hydrological budget: Spatiotemporal distribution of snowmelt and rainfall and their impact on river discharge, Journal of Geophysical Research: Earth Surface, 115, 2010.

Chatbri, H., Kameyama, K., and Kwan, P.: A comparative study using contours and skeletons as shape representations for binary image matching, Pattern Recognition Letters, 2015.

390 Chow, V.: Applied hydrology, Tata McGraw-Hill Education, 2010.

Durand, M., Gleason, C., Garambois, P.-A., Bjerklie, D., Smith, L., Roux, H., Rodriguez, E., Bates, P. D., Pavelsky, T. M., Monnier, J., et al.: An intercomparison of remote sensing river discharge estimation algorithms from measurements of river height, width, and slope, Water Resources Research, 52, 4527–4549, 2016.

Fan, J., Zeng, G., Body, M., and Hacid, M.-S.: Seeded region growing: an extensive and comparative study, Pattern recognition letters, 26,
395 1139–1156, 2005.

Frazier, P. S., Page, K. J., et al.: Water body detection and delineation with Landsat TM data, Photogrammetric Engineering and Remote Sensing, 66, 1461–1468, 2000.

Gaurav, K., Métivier, F., Devauchelle, O., Sinha, R., Chauvet, H., Houssais, M., and Bouquerel, H.: Morphology of the Kosi megafan channels, Earth Surface Dynamics Discussions, 2, 1023–1046, 2014.

400 Gaurav, K., Tandon, S., Devauchelle, O., Sinha, R., and Métivier, F.: A single width–discharge regime relationship for individual threads of braided and meandering rivers from the Himalayan Foreland, Geomorphology, 295, 126–133, 2017.

Gleason, C. J. and Smith, L. C.: Toward global mapping of river discharge using satellite images and at-many-stations hydraulic geometry, Proceedings of the National Academy of Sciences, 111, 4788–4791, 2014.

Gleason, C. J., Wada, Y., and Wang, J.: A hybrid of optical remote sensing and hydrological modeling improves water balance estimation, Journal of Advances in Modeling Earth Systems, 10, 2–17, 2018.

Glover, R. and Florey, Q.: Stable channel profiles, Hydraulic laboratory report HYD no. 325, US Department of the Interior, Bureau of Reclamation, Design and Construction Division, 1951., 1951.

Henderson, F. M.: Stability of alluvial channels, Transactions of the American Society of Civil Engineers, 128, 657–686, 1963.

Inam, A., Clift, P. D., Giosan, L., Tabrez, A. R., Tahir, M., Rabbani, M. M., and Danish, M.: The geographic, geological and oceanographic setting of the Indus River, Large rivers: geomorphology and management, pp. 333–345, 2007.

Inglis, C. C. and Lacey, G.: Meanders and their bearing on river training. Maritime and waterways engineering division., ICE Engineering Division Papers, 5, 3–24, 1947.

Kebede, M. G., Wang, L., Li, X., and Hu, Z.: Remote sensing-based river discharge estimation for a small river flowing over the high mountain regions of the Tibetan Plateau, International Journal of Remote Sensing, 41, 3322–3345, 2020.

Khan, A. A., Pant, N. C., Sarkar, A., Tandon, S., Thamban, M., and Mahalinganathan, K.: The Himalayan cryosphere: a critical assessment and evaluation of glacial melt fraction in the Bhagirathi basin, Geoscience Frontiers, 8, 107–115, 2017.

Lacey, G.: Stable channels in alluvium (Includes Appendices)., in: Minutes of the Proceedings, vol. 229, pp. 259–292, Thomas Telford, Proceedings of the Institution of Civil Engineers, Landoon, 1930.

Lam, L., Lee, S.-W., and Suen, C. Y.: Thinning methodologies-a comprehensive survey, IEEE Transactions on pattern analysis and machine intelligence, 14, 869–885, 1992.

Leopold, L. B. and Maddock, T.: The hydraulic geometry of stream channels and some physiographic implications, 1953.

Marcus, W. A. and Fonstad, M. A.: Optical remote mapping of rivers at sub-meter resolutions and watershed extents, Earth Surface Processes and Landforms, 33, 4–24, 2008.

Martinis, S., Plank, S., and Ćwik, K.: The Use of Sentinel-1 Time-Series Data to Improve Flood Monitoring in Arid Areas, Remote Sensing, 10, 583, 2018.

Mehnert, A. and Jackway, P.: An improved seeded region growing algorithm, Pattern Recognition Letters, 18, 1065–1071, 1997.

Métivier, F., Devauchelle, O., Chauvet, H., Lajeunesse, E., Meunier, P., Ashmore, P., Blanckaert, K., Zhang, Z., Fan, Y., Liu, Y., et al.: Geometry of meandering and braided gravel-bed threads from the Bayanbulak Grassland, Tianshan, PR China, Earth Surface Dynamics, 4, 273–283, 2016.

Métivier, F., Lajeunesse, E., and Devauchelle, O.: Laboratory rivers: Lacey's law, threshold theory, and channel stability, Earth Surface Dynamics, 5, 187, 2017.

Moramarco, T., Barbetta, S., Bjerklie, D. M., Fulton, J. W., and Tarpanelli, A.: River Bathymetry Estimate and Discharge Assessment from Remote Sensing, Water Resources Research, 55, 6692–6711, 2019.

Navratil, O., Albert, M.-B., Herouin, E., and Gresillon, J.-M.: Determination of bankfull discharge magnitude and frequency: comparison of methods on 16 gravel-bed river reaches, Earth Surface Processes and Landforms: The Journal of the British Geomorphological Research Group, 31, 1345–1363, 2006.

Nykanen, D. K., Foufoula-Georgiou, E., and Sapozhnikov, V. B.: Study of spatial scaling in braided river patterns using synthetic aperture radar imagery, Water resources research, 34, 1795–1807, 1998.

Papa, F., Durand, F., Rossow, W. B., Rahman, A., and Bala, S. K.: Satellite altimeter-derived monthly discharge of the Ganga-Brahmaputra
440   River and its seasonal to interannual variations from 1993 to 2008, Journal of Geophysical Research: Oceans (1978–2012), 115, 2010.

Papa, F., Bala, S. K., Pandey, R. K., Durand, F., Gopalakrishna, V., Rahman, A., and Rossow, W. B.: Ganga-Brahmaputra river discharge
       from Jason-2 radar altimetry: An update to the long-term satellite-derived estimates of continental freshwater forcing flux into the Bay of
       Bengal, Journal of Geophysical Research: Oceans (1978–2012), 117, 2012.

Passalacqua, P., Lanzoni, S., Paola, C., and Rinaldo, A.: Geomorphic signatures of deltaic processes and vegetation: The Ganges-
445   Brahmaputra-Jamuna case study, Journal of Geophysical Research: Earth Surface, 118, 1838–1849, 2013.

Rhoads, B. L.: River Dynamics: Geomorphology to Support Management, Cambridge University Press, 2020.

Ridler, T. and Calvard, S.: Picture thresholding using an iterative selection method, IEEE transactions on Systems, Man and Cybernetics, 8,
       630–632, 1978.

Schlaffer, S., Matgen, P., Hollaus, M., and Wagner, W.: Flood detection from multi-temporal SAR data using harmonic analysis and change
450   detection, International Journal of Applied Earth Observation and Geoinformation, 38, 15–24, 2015.

Schumm, S. A. and Lichty, R. W.: Time, space, and causality in geomorphology, American journal of science, 263, 110–119, 1965.

Seizilles, G.: Forme d'équilibre d'une rivière, Ph.D. thesis, Paris 7, 2013.

Seizilles, G., Devauchelle, O., Lajeunesse, E., and Métivier, F.: Width of laminar laboratory rivers, Physical Review E, 87, 052 204, 2013.

Sezgin, M. et al.: Survey over image thresholding techniques and quantitative performance evaluation, Journal of Electronic imaging, 13,
455   146–168, 2004.

Singh, P. and Jain, S.: Snow and glacier melt in the Satluj River at Bhakra Dam in the western Himalayan region, Hydrological sciences
       journal, 47, 93–106, 2002.

Smith, L., Isacks, B., Forster, R., Bloom, A., and Preuss, I.: Estimation of discharge from braided glacial rivers using ERS 1 synthetic aperture
       radar: First results, Water Resources Research, 31, 1325–1329, 1995.

460   Smith, L. C.: Satellite remote sensing of river inundation area, stage, and discharge: A review, Hydrological processes, 11, 1427–1439, 1997.

Smith, L. C. and Pavelsky, T. M.: Estimation of river discharge, propagation speed, and hydraulic geometry from space: Lena River, Siberia,
       Water Resources Research, 44, 2008.

Smith, L. C., Isacks, B. L., Bloom, A. L., and Murray, A. B.: Estimation of discharge from three braided rivers using synthetic aperture radar
       satellite imagery: Potential application to ungaged basins, Water Resources Research, 32, 2021–2034, 1996.

465   Sun, W., Ishidaira, H., and Bastola, S.: Towards improving river discharge estimation in ungauged basins: calibration of rainfall-runoff
       models based on satellite observations of river flow width at basin outlet, Hydrology and Earth System Sciences, 14, 2011, 2010.

Thayyen, R. and Gergan, J.: Role of glaciers in watershed hydrology: a preliminary study of a" Himalayan catchment", The Cryosphere, 4,
       115–128, 2010.

Twele, A., Cao, W., Plank, S., and Martinis, S.: Sentinel-1-based flood mapping: a fully automated processing chain, International Journal of
470   Remote Sensing, 37, 2990–3004, 2016.

Wolman, M. G. and Miller, J. P.: Magnitude and frequency of forces in geomorphic processes, The Journal of Geology, 68, 54–74, 1960.

Yanni, M. and Horne, E.: A new approach to dynamic thresholding, in: EUSIPCO'94: 9th European Conf. Sig. Process, vol. 1, pp. 34–44,
       1994.

Zhang, T. and Suen, C. Y.: A fast parallel algorithm for thinning digital patterns, Communications of the ACM, 27, 236–239, 1984.